

Geophysical Research Letters[®]















RESEARCH LETTER

10.1029/2022GL099611

Spatio-Temporal Structure of Far Ultraviolet Martian Dayglow Observed by EMM-EMUS

Special Section:

The First Results from the Emirates Mars Mission (EMM)

S. L. England¹ , S. Jain² , J. Deighan² , M. Chaffin² , G. Holsclaw² , J. S. Evans³ , J. Correira³ , M. O. Fillingim⁴ , R. L. Lillis⁴ , H. Almatroushi⁵ , F. Lootah⁵ , and H. Almazmi⁶ 

Key Points:

- Variations in the ultraviolet dayglow from the Martian thermosphere with local time (LT) and emission viewing angle are characterized
- Asymmetry in the dayglow between dawn and dusk varies by emission from +15.4% to −12.3% in response to transport and temperature
- Patches of significant dayglow brightness increase are observed that appear to result from changes in composition and photoelectron flux

Supporting Information:

Supporting Information may be found in the online version of this article.

Correspondence to:

S. L. England,
englands@vt.edu

Citation:

England, S. L., Jain, S., Deighan, J., Chaffin, M., Holsclaw, G., Evans, J. S., et al. (2022). Spatio-temporal structure of far ultraviolet Martian dayglow observed by EMM-EMUS. *Geophysical Research Letters*, 49, e2022GL099611. <https://doi.org/10.1029/2022GL099611>

Received 2 JUN 2022

Accepted 29 JUL 2022

Author Contributions:

Conceptualization: S. L. England, J. Deighan, J. S. Evans, R. L. Lillis

Data curation: S. Jain, J. Deighan, G. Holsclaw, J. S. Evans, J. Correira, M. O. Fillingim, H. Almatroushi, F. Lootah, H. Almazmi

Formal analysis: S. L. England

Funding acquisition: J. Deighan, R. L. Lillis, H. Almatroushi, H. Almazmi

© 2022 The Authors.

This is an open access article under the terms of the [Creative Commons Attribution-NonCommercial License](#), which permits use, distribution and reproduction in any medium, provided the original work is properly cited and is not used for commercial purposes.

¹Aerospace and Ocean Engineering, Virginia Polytechnic Institute and State University, Blacksburg, VA, USA, ²Laboratory for Atmospheric and Space Physics, University of Colorado, Boulder, Boulder, CO, USA, ³Computational Physics, Inc, Springfield, VA, USA, ⁴Space Sciences Lab, University of California, Berkeley, Berkeley, CA, USA, ⁵Mohammed Bin Rashid Space Centre, Dubai, United Arab Emirates, ⁶UAE Space Agency, Abu Dhabi, United Arab Emirates

Abstract Mars' ultraviolet dayglow has been used to study its upper atmosphere for over four decades. Identifying variations in emission features has provided information on composition, density, and temperature. The Emirates Mars Ultraviolet Spectrometer onboard the Emirates Mars Mission observes Mars' dayglow at Far and Extreme UV wavelengths. Variations in disk emission features are studied, with a focus on O I 130.4, CO Fourth Positive Group and C I 156.1 nm. All show variations with local time (LT) and emission angle as expected. Dawn-dusk asymmetry observed is attributed to LT differences in advection. Variations in the brightness of several dayglow features, including 130.4 nm, with irregular shapes are noted in around 25% of the disk images. These display some LT and hemispheric asymmetry in their occurrence rates. Examination of their spatial structure, occurrence, and spectra suggests these are associated with variations in composition and photoelectron flux.

Plain Language Summary Measurements of ultraviolet light coming from Mars' upper atmosphere has been used to measure its properties. From the color and brightness of the light, it is possible to identify both what chemical species are present in this region, their temperature and other information. The Emirates Mars Ultraviolet Spectrometer onboard the Emirates Mars Mission makes observations of this ultraviolet light in wavelength regions described as far and extreme ultraviolet. This study looks at emissions of far ultraviolet light that correspond to oxygen atoms, carbon monoxide, and carbon dioxide molecules. The circulation of gases in the upper atmosphere results in a difference in the brightness of these emissions between dawn and dusk. This study also introduces observations of irregularly shaped bright patches in these emissions. The shape, location, and spectra of these suggest they are the result of changes in the chemical composition of the upper atmosphere.

1. Introduction

Observations of ultraviolet dayglow provide information about the composition, energetics and dynamics of planetary atmospheres and ionospheres (e.g., Hendrix et al., 2014). The first of Mars were taken by Mariner 6, 7 and 9 (e.g., Barth et al., 1969; Stewart, 1972). These covered the Far and Mid ultraviolet (FUV, MUV) from ~110.0 to 430.0 nm and revealed dayglow features associated with H (Lyman alpha), O (130.4 and 135.6 nm), C (156.1 and 165.7 nm), CO (Fourth Positive Group and Cameron bands) and CO₂⁺ (Ultraviolet Doublet and Fox-Duffendack-Barker bands). Subsequently, the UV dayglow has been observed by spacecraft orbiting Mars including Mars 2 and 3 (e.g., Dementyeva et al., 1972), Mars Express (e.g., Bertaux et al., 2006), Mars Atmosphere and Volatile Evolution (MAVEN) (e.g., McClintock et al., 2014), and ExoMARS Trace Gas Orbiter (e.g., López-Valverde et al., 2018). Adding to these are observations from Earth with the extreme UV (EUV) Explorer (e.g., Krasnopolsky, 2002), Hubble Space Telescope (e.g., Bhattacharyya et al., 2017) and the Hopkins University Telescope (HUT; e.g., Feldman et al., 2000). Collectively, these have provided insight into the Martian thermosphere (e.g., Evans et al., 2015; Jain et al., 2015), and ozone (Lefèvre et al., 2021), clouds, dust and aerosols at lower altitudes (e.g., Määttänen et al., 2013; Stevens et al., 2017).

Observations of the Martian dayglow can be grouped into two categories: those made of the limb that can provide altitude profiles; and those made of the disk, which provide no altitude resolution but can offer more spatial

Methodology: S. L. England, J. S. Evans, J. Correia, R. L. Lillis

Project Administration: J. Deighan, H.

Almatroushi, H. Almazmi

Resources: G. Holsclaw

Software: S. L. England, S. Jain, G.

Holsclaw, J. Correia, R. L. Lillis

Validation: S. L. England, S. Jain, J.

Deighan, M. Chaffin, G. Holsclaw, J. S.

Evans, J. Correia, M. O. Fillingim, R.

L. Lillis, H. Almatroushi, F. Lootah, H.

Almazmi

Visualization: S. L. England, M. Chaffin

Writing – original draft: S. L. England

Writing – review & editing: J. Deighan,

M. Chaffin, J. S. Evans, R. L. Lillis

coverage per observation. At Mars, disk observations of FUV and EUV dayglow provide information on the thermosphere, owing to strong CO₂ absorption below. This study focuses on FUV disk observations.

The Emirates Mars Mission (EMM; Amiri et al., 2022) reached Mars in February 2021. From its high-altitude, 54.5 hr orbit, EMM is focused on studying the Martian atmosphere, its connection to the exosphere and atmospheric escape (Almatroushi et al., 2021). The Emirates Mars Ultraviolet Spectrometer (EMUS) is a one-dimensional imaging ultraviolet spectrometer, designed to observe the upper atmosphere and exosphere (Holsclaw et al., 2021). EMUS began taking regular science data in June 2021.

This work presents the EMM EMUS disk dayglow observations. Section 2 introduces these data, with a focus on three emission features. Section 3.1 shows the overall pattern of these features, their variation with LT and viewing angle. Section 3.2 highlights how the observed dayglow can deviate significantly from the patterns shown in Section 3.1.

2. Data

EMUS observes the Martian dayglow from 83.0–180.0 nm. The instrument design and performance are described by Holsclaw et al. (2021). The instantaneous field of view (FOV) is a narrow slit, 10.75° in the imaging direction. The disk observations used here are made from EMM's high-altitude (periapsis 19,970, apoapsis 42,650 km), 25°-inclination orbit. An image of the disk is built-up by slewing the spacecraft perpendicular to the imaging direction as a pushbroom. This is done in two operating modes, OS1 and OS2. OS1 scans take 8.9–17.4 min (from apoapsis to periapsis), utilizing the 1.3 nm resolution slit, while OS2 take 11.2–21.8 min, utilizing the 1.8 nm resolution slit. A complete image of the dayside disk is built up from two OS1 scans or three OS2 scans. An example of an OS1 is shown in Figure 1. Both OS1 and OS2 scan durations are short and have high spectral resolution, so are used interchangeably hereafter.

This study uses the Level 2B data. This L2B data is based on the L2A data, which is calibrated data in physical units derived from the L1 raw detector images in terms of counts. The data reduction process from L2A to L2B involves the multiple linear regression (MLR) fitting of reference spectra to the calibrated data, and the reference spectra are modeled from “pure” spectra. The effects from radiometric sensitivity etc. are then applied, similar to that employed for MAVEN-IUVS (Jain et al., 2015; Stevens et al., 2015). Further details on the EMUS MLR fitting are shown in Evans et al. (2022), and a comparison of the EMUS L2A spectrum to Feldman et al., 2000 is shown in Jain et al. (2022).

Three dayglow features are highlighted in this study. These are: 130.4 nm from O ³P → ³S⁰ (e.g., Barth et al., 1971; O1304 hereafter), the CO (14,4) band of the Fourth Positive Group covering ~120–180 nm (A¹Π → X¹Σ⁺; CO4PG hereafter), and 156.1 nm from C ³D⁰ → ³P (e.g., Barth et al., 1971; C1561 hereafter). O1304 comes from resonant scattering of sunlight (Stewart et al., 1992; Strickland et al., 1972, 1973), electron impact on O, CO, and CO₂ (Ajello, 1971a, 1971b; Zipf & Erdman, 1985), and photodissociative excitation of CO and CO₂ (Gentieu & Mentall, 1973; Wu & Judge, 1979). The photodissociation sources and electron impact on CO and CO₂ are negligible compared to resonant scattering and electron impact on O (Chaufray et al., 2009; Simon et al., 2009). There is also blending with CO 4PG at 130.4 nm, however the contribution is weak relative to dominant sources. The 4PG emission at 135.6 is a blend of the O I 135.6 nm doublet, the CO 4PG (14,4) band excited by solar Lyman alpha photons, and a weak contribution from the N₂ LBH (3,0) band, where the relative contributions are dictated by the local O, CO, and N₂ mixing ratios, respectively (Durrance, 1981; Kassal, 1975, 1976). Based on observations using HUT, Feldman et al. (2000) concluded that most of the observed emission at 135.6 nm is due to CO. The C1561 emission's primary excitation mechanism is photoelectron dissociative excitation of CO₂ at the airglow peak (~130 km), with a ~10% contribution from resonant scattering by C to the total column brightness (Lo et al., 2022).

Figure 1 shows an example of the three dayglow features for an OS1. In panels c–f, the vertical direction corresponds to the 10.75° instantaneous FOV. All emissions show a general decrease in brightness with increasing solar zenith angle (SZA), dropping significantly at night. Additionally, all show an increase in brightness approaching the dayside limb, corresponding to high zenith emission angles (EMA). The horizontal banding in the data that is most clear in the O1304 results from imperfections in the instrument flatfield along the imaging

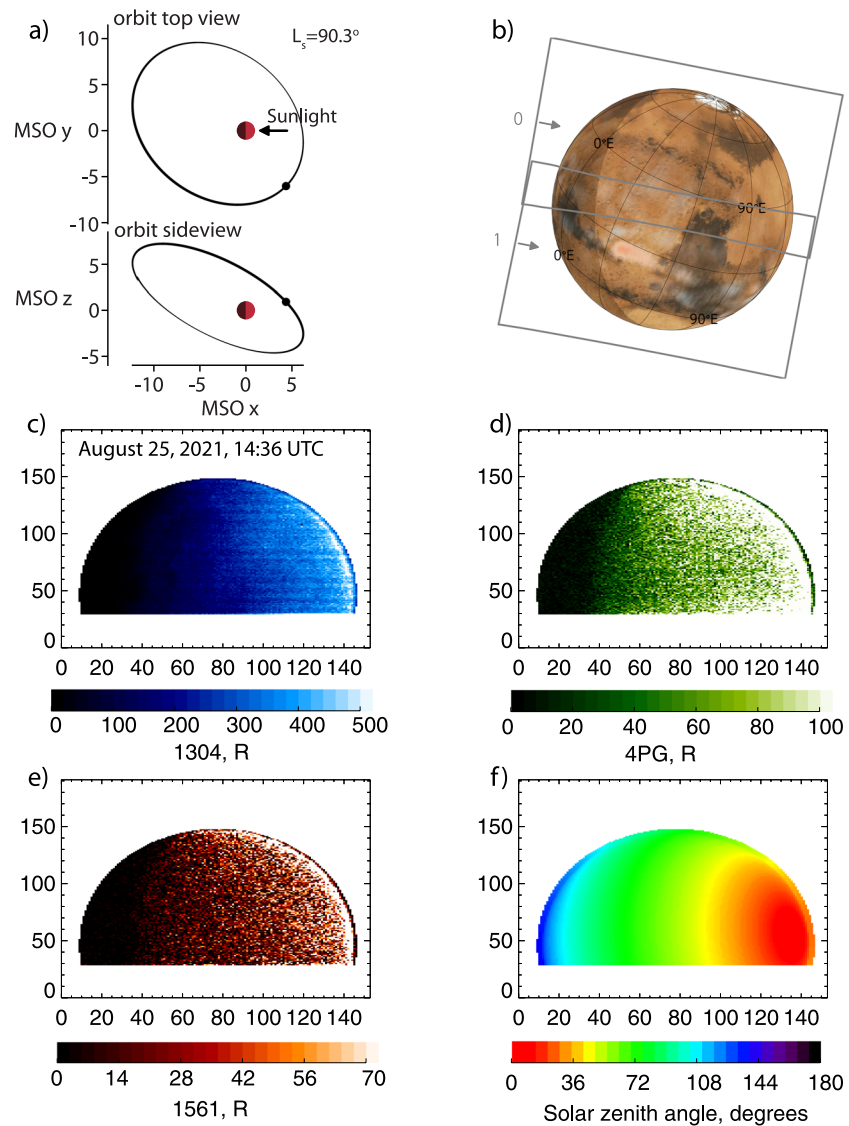


Figure 1. Example OS1 disk observation. Panels a and b show the geometry of the observation and motion of the slit as the observation is formed. Panels c through e show the brightness of O1304, CO4PG, and C1561, respectively and correspond to scan 0 in panel (b) Panel f shows the solar zenith angle of each point on the disk. In each panel, the vertical dimension corresponds to the instantaneous imaging direction and the horizontal dimension corresponds to the motion of the imaging slit. The axes correspond to the pixels in the L2B image. The horizontal banding visible in O1304 results from imperfections in the instrument flatfield along the imaging direction.

direction. These produce an $\sim 15\%$ variation for the affected pixels. It is worth noting that these imperfections appear at different locations on the disk with each observation.

The following section explores the overall variation in dayglow brightness with both EMA and LT. For this, a sequence of observations covering a wide parameter space are required. Selecting the OS1 and OS2 observations from June 11–15 September 2021 (solar longitude, $L_s = 57^\circ\text{--}99^\circ$) provides sufficient coverage, while restricting seasonal and solar EUV changes as much as possible. The MAVEN EUV monitor (EUVM) data for this time-period (Eparvier et al., 2015) reveals that the solar EUV was nearly constant, with higher flux on July 13 and 15. Excluding these days removes the effects of changing solar EUV hereafter.

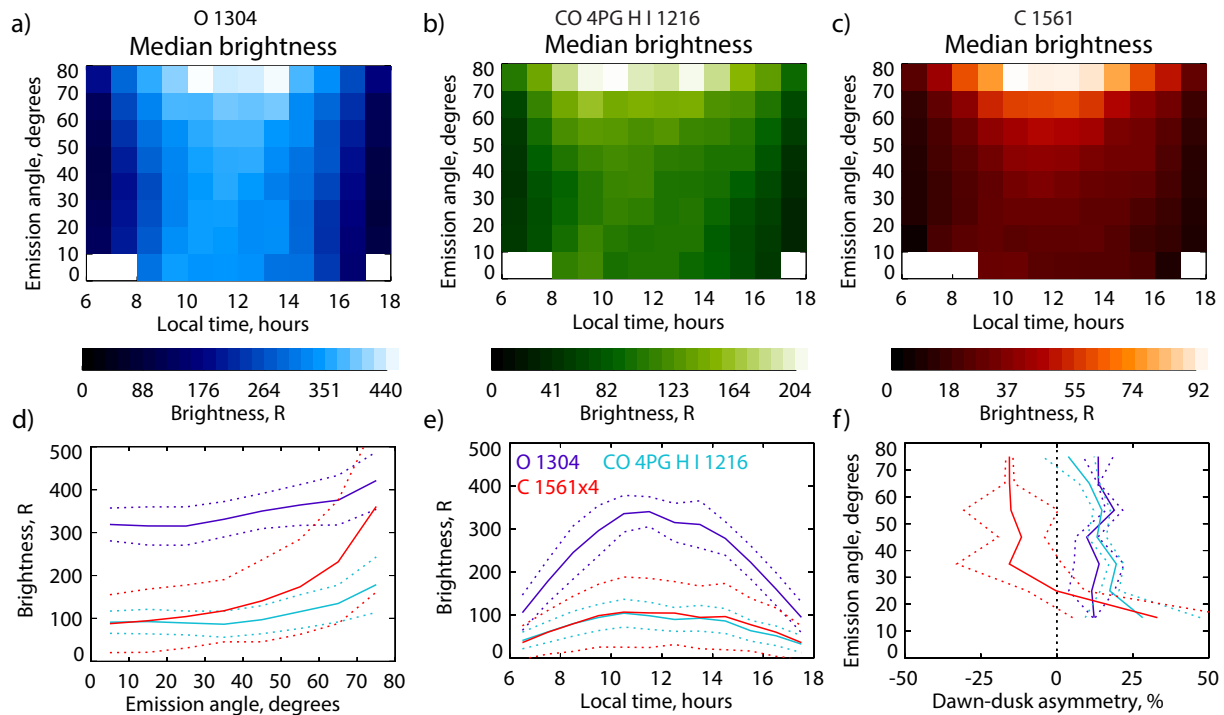


Figure 2. Panels a through c show the brightness of the O1304, CO4PG, and C1561, respectively, as functions of local time (LT) and emission angles (EMA). The median values of the emissions observed from $\pm 5^\circ$ of the equator, during June 11–15 September 2021, are shown. Panel d shows the variation in brightness at 12–13 hr LT with EMA, where the solid lines correspond to the median values and the dotted lines show the uncertainty corresponding to one standard deviation. Panel e is as panel d, but for the values from 20–30° EMA, as a function of LT. C1561 has been increased by a factor of 4 in panels d and e for clarity. Panel f shows the dawn-dusk asymmetry in the brightness of the emissions. Here, dawn corresponds to 7–8 hr LT, and dusk to 16–17 hr LT. The percent values correspond to (dawn-dusk)/dusk.

3. Method and Results

3.1. Variation With LT and EMA

To investigate the variation in the dayglow with LT and EMA, all OS1 and OS2 data described in Section 2 are used. As the L_s range is close to northern summer solstice, only data from $\pm 5^\circ$ latitude are included, leaving only variations in LT and EMA (removing SZA effects that are not accounted for by LT). All data are then binned into 1 hr by 10° bins for $EMA \leq 80^\circ$ (avoiding the limb). Figure 2, panels a–c show the average (median) brightness of the three dayglow features as functions of LT and EMA. The general variation is as expected, with the brightest dayglow in all three emissions seen near local noon, and at higher EMA (corresponding to longer viewing path lengths through the dayglow layer). Figure 2, panels d and e show this in more detail, where panel d shows the variation with EMA in all three emissions at 12–13 hr LT and panel e shows the variation with LT at 20–30° EMA. Both the median and one standard deviation ranges (resulting from both geophysical variations and measurement uncertainty) are shown. The variation with EMA shows an increase in all three emissions, but the relative increase for C1561 is notably larger.

The variation with LT is similar for all three, with some morning–afternoon asymmetry visible. To investigate the morning–afternoon asymmetry in more detail, data close to dawn and dusk are selected. Here 7–8 LT is used to represent dawn and 16–17 LT for dusk to avoid the extremely low signal at the terminator, especially in the C1561 emission. The dawn-dusk asymmetry is shown in Figure 2, panel f. Both the O1304 and CO4PG emissions show similar behavior, with dawn being $\sim 10\%$ – 20% brighter than dusk at all EMA. The C1561 emission shows a distinctly different behavior, showing generally the opposite trend at most EMA, except for the very lowest. The positive asymmetry in C1561 in the 10–20° EMA bin should perhaps be viewed with caution as the dawn 10–20° EMA bin contains one tenth the number samples than any other, and the largest uncertainty of any point. Excluding this bin, the average asymmetry for O1304 is $13.5\% \pm 3.1\%$, for CO4PG is $15.4\% \pm 7.6\%$, and for C1561 is $-12.3\% \pm 6.1\%$.

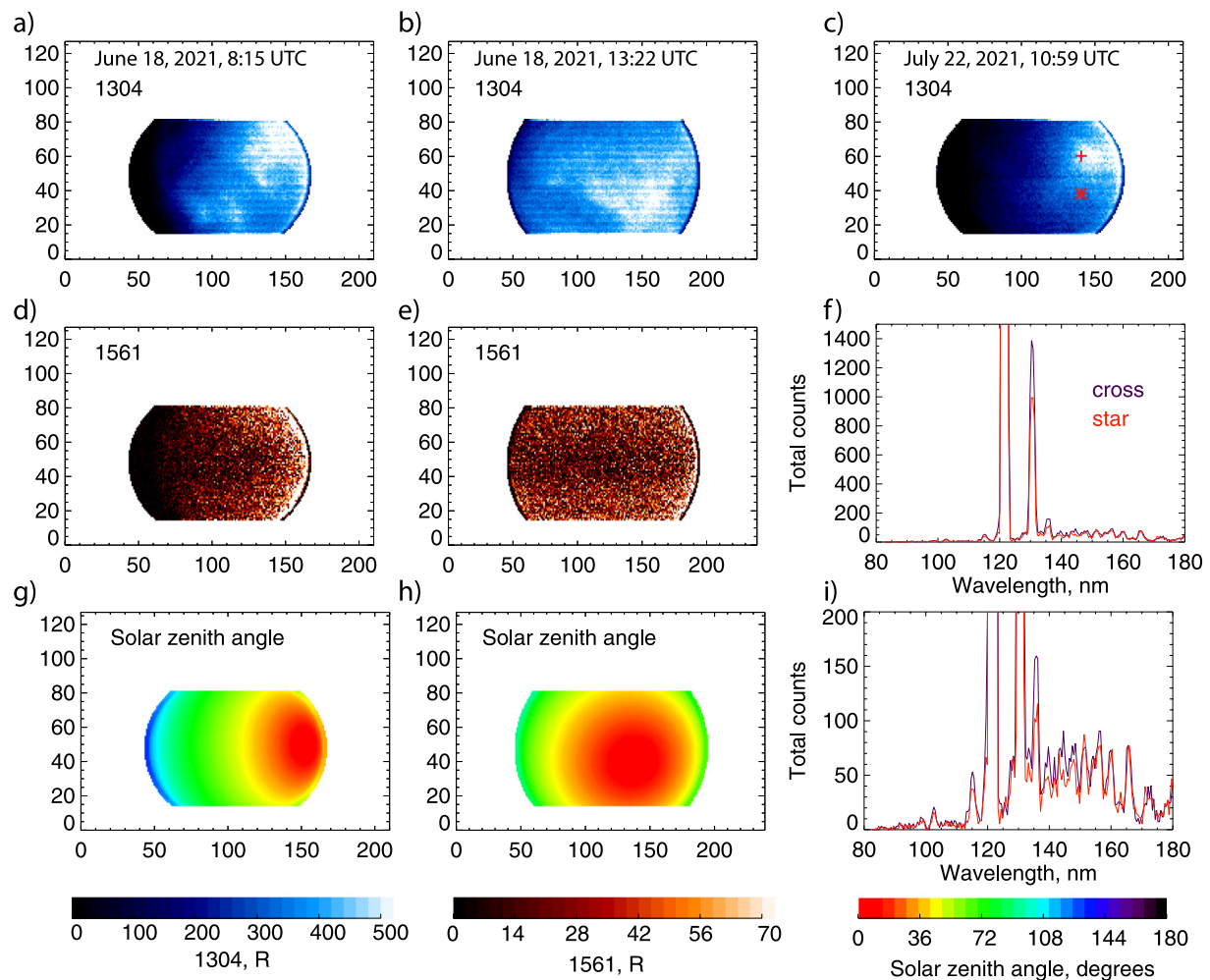


Figure 3. Examples of irregularly shaped dayglow variations. The left two columns correspond to a pair of observations on the same day. The brightness of O1304 and C1561 are shown, along with the corresponding solar zenith angle (SZA) for each image. The irregularly shaped variations are clear in O1304 emission in both cases, and absent in C1561. Panel c shows another example of an irregularly shaped variation in O1304. The cross corresponds to a point at 26° SZA, 39° emission angles (EMA), and the star is at 28° SZA, 38° EMA. The same spectrum is shown in panels f and i, corresponding to sum of nine pixels around the cross and star shown in panel c.

3.2. Irregularly-Shaped Dayglow Variations

While the previous section showed the average variations in the dayglow with EMA and LT, this section focuses on notable departures from this behavior, where the variation in the brightness of the dayglow cannot be explained by geometric effects such as LT, SZA and EMA. Perhaps the most clearly visible of these are large ($>10^\circ$ on the disk) regions where some of the dayglow features are significantly brighter than expected, which occur in some of the disk scans. Figure 3 shows several examples of this. The left and central columns show examples from 18 June 2021, taken approximately 5 hr apart. The irregularly shaped bright features in O1304 are evident in both, with shapes and locations that do not follow either EMA or SZA. No similar features are evident in C1561. For a closer examination of the spectral differences between regions exhibiting this brightening in some dayglow features, the right column of Figure 3 shows an example from 22 July 2021. In this example, the geometry of the observation provides the opportunity to sample two regions of the disk with almost identical SZA and EMA, one inside the bright region of O1304 and one outside (identified by the star and cross symbols). Panels f and i show the spectra averaged over nine points around these two locations (to provide sufficient signal in the dimmer features). It can be seen from panel f that the brightness of O1304 is 40% higher inside this region than the comparable location outside, which is well beyond the variation expected from the patterns shown in Figure 2, instrument noise etc. Panel i shows that these variations are strongly dependent on wavelength, with some showing large increases

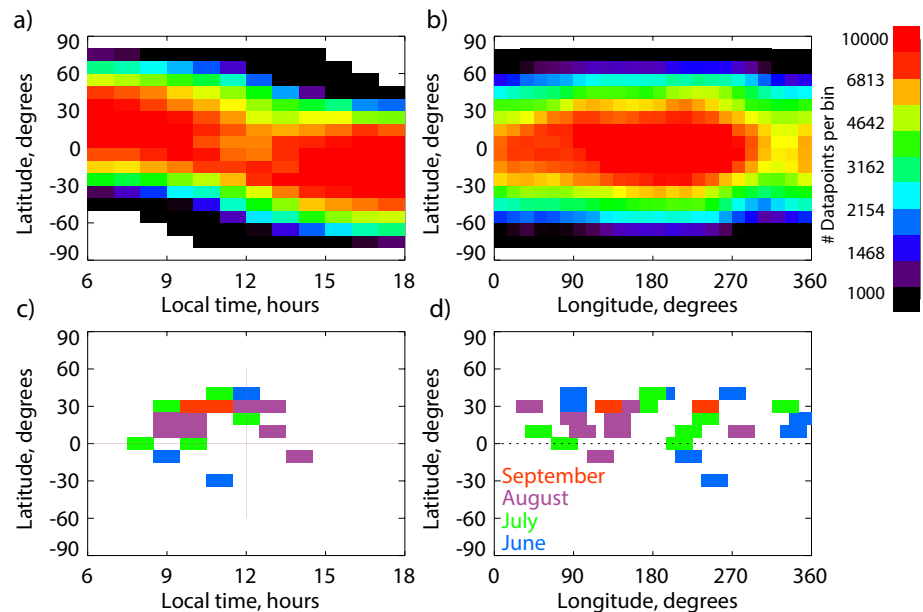


Figure 4. Distribution of the dayglow observations, and approximate locations of the irregularly shaped bright features seen in O1304. Panels a and b show the number of observations from June 11–15 September 2021, as functions of latitude and local time (LT) and latitude and longitude, respectively. Panels c and d show the approximate locations of the irregularly shaped bright features. The color-coding corresponds to the month of the observation. Note that some locations overlap, such as near 9–11 hr LT, 10–30° north in panel d. A complete listing of the locations and dates is given in Supporting Information S1.

such as the blended feature at 135.6 nm and the CO Hopfield-Birge (B-X) (0,0) band near 115.0 nm (which is expected to behave similarly to the CO4PG as both are produced by thermal CO), while others see almost no change, including C1561 and the CI feature at 165.7 nm, both of which are primary generated by electron impact dissociation of CO₂ (e.g., Lo, et al., 2022).

Examining a number of the irregularly shaped bright features in the O1304 emission, a wide range of shapes, sizes and locations are seen. These occur sporadically. To make progress in identifying potential sources of these features, the times and locations of these features have been identified. As each feature has a different, amorphous shape, this identification has been done by eye. While this approach is potentially impacted by human subjectivity, it offers a useful starting point before a more rigorous algorithm can be developed. For this, all of the O1304 images during the 3 months considered were examined, and the presence of bright features occurring away from the limb that were not related to SZA, or EMA were noted, along with their approximate central location and LT. A complete list of these is given in Supporting Information S1.

Panels c and d of Figure 4 shows the distribution of the irregularly shaped bright features identified. To interpret this distribution, it is important to consider the sampling distribution within the date range used, which is shown in Figure 4, panels a and b. The distribution with latitude and longitude shows a greater concentration of data points at low latitude, with a drop-off beyond $\pm 45^\circ$ latitude. The distribution of data with latitude and LT is uneven and must be taken into account. Noting these trends, the distribution of the occurrences of irregularly shaped bright features are shown in Figure 4, panels c and d. Panel d shows a clear hemispheric asymmetry in the occurrence rate of these features, with a higher occurrence rate in the northern hemisphere. No preferred longitude range is evident. Panel c shows a clear LT asymmetry, with a higher occurrence rate before local noon. Re-examining panel a, some amount of asymmetry is expected, as during the pre-noon hours there are more data available in the north than the south. Thus, if either the pre-noon or northern-hemisphere trends are real, the other may be seen in these plots. Looking at this in more detail, the asymmetry in the data availability at $\pm 30^\circ$ latitude at 9 LT is a factor of ~ 3 . The asymmetry in the data availability at $+30^\circ$ latitude between 9 LT and 15 LT is a factor of ~ 2 . The recorded asymmetry in the occurrence rate between north and south, and pre- and post-noon are both about a factor 7. This suggests that the observed asymmetry is not simply an artifact of the sampling, although with a relatively small sample size it is not clear how strong the true asymmetry is.

4. Discussion and Conclusions

The equatorial disk brightness of three dayglow features (O 130.4 nm, Lyman-Alpha pumped CO 4PG, and C 156.1 nm) are examined for data from June 11–15 September 2021 ($L_s = 57^\circ\text{--}99^\circ$). Focusing on the median brightness, that are not significantly affected by the irregularly shaped variations considered below, the following can be understood:

1. The brightness of all three dayglow features respond most directly to the angle to the Sun (LT and/or SZA) and EMA. All three follow the same basic pattern of becoming brighter at lower SZA, and higher EMA, consistent with the changes in solar EUV input and ray path length through the emitting layer. The variations in CO4PG and O1304 are the most similar. The C1561 emission varies more strongly with EMA and varies in the opposite manner between near dawn and near dusk.
2. The change in brightness of the three emissions between low and high EMA are not the same. For O1304, the variation between 5° and 75° EMA is about a factor of 1.3, for CO4PG it is about a factor of 2 and for C1561 it is about a factor of 4. For optically thin emissions such as C1561, the increase with EMA is consistent with the varying ray path length through a slab emitting layer (following $1/\cosine$ (EMA)). For the optically thick O1304 and CO4PG, further interpretation would require more detailed modeling.
3. Focusing on the differences near dawn and dusk, O1304 and CO4PG display a similar degree of asymmetry, with dawn brighter than dusk at all EMA (averaging $13.5\% \pm 3.1\%$ and $15.4\% \pm 7.6\%$, respectively). Assuming that the brightness of the O1304 and CO4PG emissions at a particular latitude, SZA and EMA is governed by the column ratios of O/CO₂ and CO/CO₂ in the thermosphere respectively (as they are produced by resonant scattering of sunlight by O and CO, and absorbed by CO₂), the observed asymmetry can be attributed to the influence of advection on the composition of the thermosphere that is believed to also produce asymmetries in He/CO₂ between dawn and dusk (e.g., Elrod et al., 2017; Gupta et al., 2021). Quantifying this compositional asymmetry for these optically thick emissions would require modeling that is beyond the scope of this paper. Across most EMA, C1561 displays the opposite dawn-dusk asymmetry (average of $-12.3\% \pm 6.1\%$). This is understood as an increase in CO₂ leads to a decrease in O1304 and CO4PG via absorption, but an increase in C1561 via higher photoelectron dissociative excitation of CO₂.

EMUS offers the first synoptic view of the Martian thermosphere in the FUV. Examining the disk images, around one quarter of the O1304 images display irregularly shaped variations in brightness that are not simply related to geometry. These patches of brighter dayglow span 10° across the disk, have amorphous shapes, and occur sporadically throughout the data set.

1. The irregularly shaped bright features only appear in some dayglow features, and are perhaps clearest in O1304 as a result of its high signal-to-noise ratio (SNR), and the fact that the brighter spots are $>10\%$ brighter than otherwise comparable regions. Variations in O1304 are known to result from a variety of processes. The origin in this case is unlikely to be instrumental noise, as they greatly exceed the SNR (the cross compared to the star in Figure 3c corresponds to an SNR of 19), are coherent across many adjacent pixels, and show up at comparable strengths in several wavelengths. They are unlikely to be associated with true temporal changes in solar EUV flux, both as this is largely constant through the dates analyzed and as any sudden change in solar EUV (e.g., from a flare) would create a signature that is aligned with the vertical direction (the instantaneous FOV) in the images shown (which is not the case e.g., Figure 3), and would not show up in successive images of the planet taken around 5 hr apart (Figures 3a and 3b). They are unlikely to be associated with precipitating electrons as they show no apparent correspondence to the crustal magnetic field regions (e.g., Brain et al., 2003; Connerney et al., 2001), and the magnitude of the signature seen (e.g., in O1304) is an order of magnitude larger than that seen in auroral signatures on the nightside (Lillis et al., 2022). Following the above process of elimination and concluding that these variations are both real, and not caused by external factors that modulate the dayglow production rate leaves real thermospheric variations as the most likely cause of these features. Variations in thermospheric temperatures and composition have been reported from both remote and in situ observations (e.g., England et al., 2016; Jain et al., 2015). While a detailed analysis of the response of each emission to changing composition and photoelectron flux is beyond the scope of this paper, it is known that the production of photoelectrons at Mars is highly variable, and likely the result of changes in thermospheric composition (e.g., Lillis et al., 2021). Thus, one plausible explanation for the irregularly shaped bright features in the dayglow is changes in the thermospheric composition, perhaps amplified in terms of relative changes in the emission brightness via modulation of the photoelectron flux in the vicinity of the

dayglow peak. The variable response at different wavelengths is then plausibly the result of changes in the composition of the thermosphere.

2. Exploring the spatial and temporal distribution of the irregularly shaped features in O1304, the highest occurrence rates are seen in the northern hemisphere, before noon. Further data would be required to determine if this is always the case, or more simply reflects the limited L_s range examined here. No preferred longitude or latitude, beyond generally northern hemisphere, is apparent. The underlying cause of this remains unknown. Assuming that these features are associated with a real variation in thermospheric composition, interacting with varying photoelectron flux, further observations and modeling of the composition and resultant dayglow will likely be required to fully understand the nature of these features. The sporadic occurrence of these features may contribute to why they have not been reported in prior observations from Mars, but perhaps reexamination of these data will now yield further understanding of these features.

Data Availability Statement

The EMUS Level 2B data used in this study are available at the Emirate Mars Mission Science Data Center at <https://sdc.emiratesmarsmission.ae/data/emus>. This location is designated as the primary repository for all data products produced by the EMM team and is designated as long-term repository as required by the UAE Space Agency. Software to read the L2B files is also provided at the EMM repository. Extreme UV monitor Level 2 data used are available at the Planetary Data System (PDS) Planetary Plasma Interactions Node, <https://pds-ppi.igpp.ucla.edu/mission/MAVEN/MAVEN/EUV>. The locations of each point in Figure 4 are provided in Table S1 of Supporting Information S1.

Acknowledgments

Funding for development of the Emirates Mars mission was provided by the UAE government, and to co-authors outside of the UAE by MBRSC.

References

- Ajello, J. M. (1971a). Emission cross sections of CO by electron impact in the interval 1260–5000 Å. I. *The Journal of Chemical Physics*, 55(7), 3158–3168. <https://doi.org/10.1063/1.1676563>
- Ajello, J. M. (1971b). Emission cross sections of CO₂ by electron impact in the interval 1260–4500 Å. II. *The Journal of Chemical Physics*, 55(7), 3169–3177. <https://doi.org/10.1063/1.1676564>
- Almatroushi, H., AlMazmi, H., AlMheiri, N., AlShamsi, M., AlTunajji, E., Badri, K., et al. (2021). Emirates Mars mission characterization of Mars atmosphere dynamics and processes. *Space Science Reviews*, 217(8), 89. <https://doi.org/10.1007/s11214-021-00851-6>
- Amiri, H. E. S., Brain, D., Sharaf, O., Withnell, P., McGrath, M., Alloghani, M., et al. (2022). The emirates Mars mission. *Space Science Reviews*, 218(1), 4. <https://doi.org/10.1007/s11214-021-00868-x>
- Barth, C. A., Fastie, W. G., Hord, C. W., Pearce, J. B., Kelly, K. K., Stewart, A. I., et al. (1969). Mariner 6 and 7: Ultraviolet spectrum of Mars upper atmosphere. *Science*, 165(3897), 1004–1005. <https://doi.org/10.1126/science.165.3897.1004>
- Barth, C. A., Hord, C. W., Pearce, J. B., Kelly, K. K., Anderson, G. P., & Stewart, A. I. (1971). Mariner 6 and 7 ultraviolet spectrometer experiment: Upper atmosphere data. *Journal of Geophysical Research*, 76, 10–2227. <https://doi.org/10.1029/JA076i010p02213>
- Bertaux, J. L., Korabiev, O., Perrier, S., merais, E. Q., Montmessin, F., Leblanc, F., et al. (2006). SPICAM on Mars express: Observing modes and overview of UV spectrometer data and scientific results. *Journal of Geophysical Research*, 111, 10. <https://doi.org/10.1029/2006JE002690>
- Bhattacharyya, D., Clarke, J. T., Chaufray, J. Y., Mayyasi, M., Bertaux, J. L., Chaffin, M. S., et al. (2017). Seasonal changes in hydrogen escape from Mars through analysis of HST observations of the Martian exosphere near perihelion. *Journal of Geophysical Research: Space Physics*, 122, 11756–11764. <https://doi.org/10.1002/2017JA024572>
- Brain, D. A., Bagenal, F., Acuña, M. H., & Connerney, J. E. P. (2003). Martian magnetic morphology: Contributions from the solar wind and crust. *Journal of Geophysical Research*, 108(A12), 1424. <https://doi.org/10.1029/2002JA009482>
- Chaufray, J. Y., Leblanc, F., Quémerais, E., & Bertaux, J. L. (2009). Martian oxygen density at the exobase deduced from OI 130.4-nm observations by spectroscopy for the investigation of the characteristics of the atmosphere of Mars on Mars express. *Journal of Geophysical Research*, 114, E02006. <https://doi.org/10.1029/2008je003130>
- Connerney, J. E. P., Acuña, M. H., Wasilewski, P. J., Kletetschka, G., Ness, N. F., Rème, H., et al. (2001). The global magnetic field of Mars and implications for crustal evolution. *Geophysical Research Letters*, 28(21), 4015–4018. <https://doi.org/10.1029/2001GL013619>
- Dementyeva, N. N., Kurt, V. G., Smirnov, A. S., Titarchuk, L. G., & Chuvahin, S. D. (1972). Preliminary results of measurements of UV emissions scattered in the Martian upper atmosphere. *Icarus*, 17(2), 475–483. [https://doi.org/10.1016/0019-1035\(72\)90013-9](https://doi.org/10.1016/0019-1035(72)90013-9)
- Durrance, S. T. (1981). The carbon monoxide fourth positive bands in the Venus dayglow 1. Synthetic spectra. *Journal of Geophysical Research*, 86(A11), 9115–9124. <https://doi.org/10.1029/ja086a11p09115>
- Elrod, M. K., Bougher, S., Bell, J., Mahaffy, P. R., Benna, M., Stone, S., et al. (2017). He bulge revealed: He and CO₂ diurnal and seasonal variations in the upper atmosphere of Mars as detected by MAVEN NGIMS. *Journal of Geophysical Research: Space Physics*, 122, 2564–2573. <https://doi.org/10.1002/2016JA023482>
- England, S. L., Liu, G., Withers, P., Yigit, E., Lo, D., Jain, S., et al. (2016). Simultaneous observations of atmospheric tides from combined in situ and remote observations at Mars from the MAVEN spacecraft. *Journal of Geophysical Research: Planets*, 121, 594–607. <https://doi.org/10.1002/2016JE004997>
- Eparvier, F., Chamberlin, P. C., Woods, T. N., & Thiemann, E. M. B. (2015). The solar extreme ultraviolet monitor for MAVEN. *Space Science Reviews*, 195(1–4), 293–301. <https://doi.org/10.1007/s11214-015-0195-2>
- Evans, J. S., Correia, J., Deighan, J., Jain, S., Al Matroushi, H., Al Mazmi, H., et al. (2022). Retrieval of CO relative column abundance in the Martian thermosphere from FUV disk observations by EMM EMUS. *Geophysical Research Letters*, 49, e2022GL099615. <https://doi.org/10.1029/2022GL099615>

- Evans, J. S., Stevens, M. H., Lumpe, J. D., Schneider, N. M., Stewart, A. I. F., Deighan, J., et al. (2015). Retrieval of CO₂ and N₂ in the Martian thermosphere using dayglow observations by IUVS on MAVEN. *Geophysical Research Letters*, 42(21), 9040–9049. <https://doi.org/10.1002/2015GL065489>
- Feldman, P. D., Burgh, E. B., Durrance, S. T., & Davidsen, A. F. (2000). Far-ultraviolet spectroscopy of Venus and Mars at 4 Å resolution with the Hopkins ultraviolet telescope on Astro-2. *The Astrophysical Journal*, 538(1), 395–400. <https://doi.org/10.1086/309125>
- Gentieu, E. P., & Mentall, J. E. (1973). Cross sections for production of the CO (A 1 Π– X 1 Σ) fourth positive band system and O (3 S) by photodissociation of CO₂. *The Journal of Chemical Physics*, 58(11), 4803–4815. <https://doi.org/10.1063/1.1679063>
- Gupta, N., Rao, N. V., Bougher, S., & Elrod, M. K. (2021). Latitudinal and seasonal asymmetries of the helium bulge in the Martian upper atmosphere. *Journal of Geophysical Research: Planets*, 126, e2021JE006976. <https://doi.org/10.1029/2021je006976>
- Hendrix, A. R., Nelson, R. M., & Domingue, D. L. (2014). In T. Spohn, D. Breuer, & T. V. Johnson (Eds.), *Chapter 49 - the solar system at ultraviolet wavelengths, Encyclopedia of the solar system* (3rd ed., pp. 1047–1071). Elsevier. <https://doi.org/10.1016/B978-0-12-415845-0.00049-9>
- Holsclaw, G. M., Deighan, J., Almatroushi, H., Chaffin, M., Correia, J., Evans, J. S., et al. (2021). The emirates Mars ultraviolet spectrometer (EMUS) for the EMM mission. *Space Science Reviews*, 217(8), 79. <https://doi.org/10.1007/s11214-021-00854-3>
- Jain, S. K., Deighan, J., Chaffin, M., Holsclaw, G., Lillis, R., Fillingim, M., et al. (2022). Morphology of extreme and far ultraviolet Martian airglow emissions observed by the EMUS instrument on board the Emirates Mars Mission. *Geophysical Research Letters*, 49, e2022GL099885. <https://doi.org/10.1029/2022GL099885>
- Jain, S. K., Stewart, A. I. F., Schneider, N. M., Deighan, J., Stiepen, A., Evans, J. S., et al. (2015). The structure and variability of Mars upper atmosphere as seen in MAVEN/IUVS dayglow observations. *Geophysical Research Letters*, 42(21), 9023–9030. <https://doi.org/10.1002/2015GL065419>
- Kassal, T. (1975). Resonant fluorescent scattering of solar radiation by the fourth positive band system of CO. *Applied Optics*, 14(7), 1513–1515. <https://doi.org/10.1364/AO.14.001513>
- Kassal, T. T. (1976). Scattering of solar Lyman alpha by the (14, 0) band of the fourth positive system of CO. *Journal of Geophysical Research*, 81(7), 1411–1412. <https://doi.org/10.1029/JA081i007p01411>
- Krasnopolsky, V. A. (2002). Mars' upper atmosphere and ionosphere at low, medium, and high solar activities: Implications for evolution of water. *Journal of Geophysical Research*, 107, 5128. <https://doi.org/10.1029/2001JE001809>
- Lefèvre, F., Trokhimovskiy, A., Fedorova, A., Baggio, L., Lacombe, G., Maattanen, A., et al. (2021). Relationship between the ozone and water vapour columns on Mars as observed by SPICAM and calculated by a global climate model. *Journal of Geophysical Research: Planets*, 126, e2021JE006838. <https://doi.org/10.1029/2021JE006838>
- Lillis, R. J., Deighan, J., Brain, D., Fillingim, M., Jain, S., Chaffin, M., et al. (2022). First synoptic images of FUV discrete aurora and discovery of sinuous aurora at Mars by EMM EMUS. *Geophysical Research Letters*, 49, e2022GL099820. <https://doi.org/10.1029/2022GL099820>
- Lillis, R. J., Xu, S., Mitchell, D., Thiemann, E., Eparvier, F., Benna, M., & Elrod, M. (2021). Ionization efficiency in the dayside ionosphere of Mars: Structure and variability. *Journal of Geophysical Research: Planets*, 126, e2021JE006923. <https://doi.org/10.1029/2021JE006923>
- Lo, D. Y., Yelle, R. V., Deighan, J. I., Jain, S. K., Evans, J. S., Stevens, M. H., et al. (2022). MAVEN/IUVS observations of C I 156.1 nm and 165.7 nm dayglow: Direct detection of carbon and implication on photochemical escape. *Icarus*, 371, 114664. <https://doi.org/10.1016/j.icarus.2021.114664>
- López-Valverde, M. A., Gerard, J. C., González-Galindo, F., Vandaele, A. C., Thomas, I., Korabiev, O., et al. (2018). Investigations of the Mars upper atmosphere with ExoMars trace gas orbiter. *Space Science Reviews*, 214(1), 29. <https://doi.org/10.1007/s11214-017-0463-4>
- Määttä, A., Listowski, C., Montmessin, F., Maltagliati, L., Reberac, A., Joly, L., & Bertaux, J.-L. (2013). A complete climatology of the aerosol vertical distribution on Mars from MEX/SPICAM UV solar occultations. *Icarus*, 223(2), 892–941. <https://doi.org/10.1016/j.icarus.2012.12.001>
- McClintock, W. E., Schneider, N. M., Holsclaw, G. M., Clarke, J. T., Hoskins, A. C., Stewart, I., et al. (2014). The imaging ultraviolet spectrograph (IUVS) for the MAVEN mission. *Space Science Reviews*, 195(1–4), 75–124. <https://doi.org/10.1007/s11214-014-0098-7>
- Simon, C., Witasse, O., Leblanc, F., Gronoff, G., & Bertaux, J. L. (2009). Dayglow on Mars: Kinetic modelling with SPICAM UV limb data. *Planetary and Space Science*, 57(8–9), 1008–1021. <https://doi.org/10.1016/j.pss.2008.08.012>
- Stevens, M. H., Evans, J. S., Schneider, N. M., Stewart, A. I. F., Deighan, J., Jain, S. K., et al. (2015). N₂ in the upper atmosphere of Mars observed by IUVS on MAVEN. *Geophysical Research Letters*, 42(21), 9050–9056. <https://doi.org/10.1002/2015GL065319>
- Stevens, M. H., Siskind, D. E., Evans, J. S., Jain, S. K., Schneider, N. M., Deighan, J., et al. (2017). Martian mesospheric cloud observations by IUVS on MAVEN: Thermal tides coupled to the upper atmosphere. *Geophysical Research Letters*, 44(10), 4709–4715. <https://doi.org/10.1002/2017GL072717>
- Stewart, A. I. (1972). Mariner 6 and 7 ultraviolet spectrometer experiment: Implication of CO₂, CO, and O airglow. *Journal of Geophysical Research*, 77(1), 54–68. <https://doi.org/10.1029/JA077i001p00054>
- Stewart, A. I. F., Alexander, M. J., Meier, R. R., Paxton, L. J., Bougher, S. W., & Fesen, C. G. (1992). Atomic oxygen in the Martian thermosphere. *Journal of Geophysical Research*, 97(A1), 91–102. <https://doi.org/10.1029/91ja02489>
- Strickland, D. J., Stewart, A. I., Barth, C. A., Hord, C. W., & Lane, A. L. (1973). Mariner 9 ultraviolet spectrometer experiment: Mars atomic oxygen 1304-Å emission. *Journal of Geophysical Research*, 78(22), 4547–4559. <https://doi.org/10.1029/ja078i022p04547>
- Strickland, D. J., Thomas, G. E., & Sparks, P. R. (1972). Mariner 6 and 7 ultraviolet spectrometer experiment: Analysis of the OI 1304- and 1356-Å emissions. *Journal of Geophysical Research*, 77(22), 4052–4068. <https://doi.org/10.1029/ja077i022p04052>
- Wu, C. R., & Judge, D. L. (1979). The atomic oxygen 1304 Å emission produced through photodissociation of CO and CO₂. *Chemical Physics Letters*, 68(2–3), 495–498. [https://doi.org/10.1016/0009-2614\(79\)87245-0](https://doi.org/10.1016/0009-2614(79)87245-0)
- Zipf, E. C., & Erdman, P. W. (1985). Electron impact excitation of atomic oxygen: Revised cross sections. *Journal of Geophysical Research*, 90(A11), 11087–11090. <https://doi.org/10.1029/JA090iA11p11087>